

Bonding Properties of Manganese Nitrides at High Pressure and the Discovery of MnN₄ with planar N₄ rings

Li Li¹, Kuo Bao^{1*}, Xingbin Zhao¹, and Tian Cui^{2,1*}

¹State Key Laboratory of Superhard Materials, College of Physics, Jilin University, Changchun, 130012, China

²Institute of High Pressure Physics, School of Physical Science and Technology, Ningbo University, Ningbo 315211, China;

*Corresponding authors: baokuo@jlu.edu.cn, and cuitian@nbu.edu.cn

Abstract

It is not easy to synthesize high quality manganese nitrides experimentally; however, owing to the intrinsic characteristics of manganese and nitrogen, these materials possess remarkable properties and have highly promising applications. In this study, we systematically examined the stoichiometric phase spaces of Mn–N compounds from 0 to 100 GPa using *ab initio* calculations and constructed a high-pressure magnetic phase diagram. Remarkably, N-rich MnN₄ with a planar N₄ ring was discovered for the first time in the pressure range of 40–100 GPa. The electronic structures revealed that the N₄ ring is formed by the *sp*² hybridization of nitrogen atoms. Furthermore, its superconducting transition temperature is approximately 1.6 K, and its bulk modulus is 381 GPa, thereby rendering it a potential hard superconductive material. Moreover, we determined a new phase transition sequence for MnN: the semi-conducting non-magnetic (NM) *zb* phase (5 GPa) first transforms to metallic antiferromagnetic (AFM) *NiAs* (40 GPa), which further transforms to the more stable metallic ferromagnetic (FM) *rs* phase. The mechanical properties indicated that covalent interactions have a significant effect on the hardness of the N-rich structures and almost no effect on the Mn-rich structures in Mn–N compounds. Our work provides an overview of the Mn–N compounds and their properties under pressure and presents an updated phase diagram.

Keywords: Transition metal nitrides; Superconductivity; Mechanical properties; Electronic properties; Magnetic properties

Introduction

Manganese is a unique transition metal (TM), not only because it has the highest magnetic moment among all the elements, but also because it has one of the highest electron densities. Thus, its compounds have also drawn considerable attention owing to their magnetic, electronic, semi conductive, superconductive, and photovoltaic behaviors. Parallely, nitrogen shows interesting structures and behavior under high pressure (HP).^{1, 2} Thus, manganese nitrides possess remarkable properties and have promising applications. However, the synthesis of “pure” TM nitrides or compounds with an integral ratio is a challenge using the conventional methods, because nitrogen ($N \equiv N$) is highly stable and unreactive. The use of HP is an effective and clean method to change hybridization modes, bonding ways, and valence electron orbitals and to synthesize novel materials with special physicochemical properties. A series of poly-nitrogen forms have been predicted and synthesized at HP.³⁻¹⁰ In addition to high energy density materials, TM nitrides have been drawing considerable attention owing to their outstanding mechanical,¹¹ superconductive, and magnetic properties under certain conditions. TiN was synthesized as a superconducting film that underwent disorder-driven superconductor–insulator transition.¹² NbN^{13, 14} and MoN,¹⁵ both of which are ultra-hard and superconducting unconventional functional nitrides, have been reported. Several studies have shown that different bonding patterns between nitrogen atoms have significant influence on the mechanical properties of materials. In the Fe–N system, the hardness of Fe₃N₈ and FeN₃ with N chains was measured to be above 30 GPa.¹⁶ Recently, trigonal WN₆ with armchair-like hexazine (N₆) rings was synthesized, and its hardness was determined to be 57.9 GPa by theoretical calculations.¹⁷ The N₂ units in CrN₂, TiN₂, IrN₂ and OsN₂ have been shown to impart ultra-incompressible properties with high bulk modulus (B) and shear modulus (G).^{11, 18}

Mn–N compounds manifest rich magnetic phases. Until now, the ϵ -Mn₄N, ζ -Mn₂N, θ -MnN, and η -Mn₃N₂ phases have been synthesized¹⁹⁻²¹. Face-centered cubic ϵ -Mn₄N exhibits interesting ferrimagnetic (FiM) order magnetism; the magnetic moment of Mn on the corner (Mn-I) is 3.3 μ_B and antiparallel to the three Mn (Mn-II) on face center is 0.7 μ_B ²². It exhibits a distinct anomalous Hall Effect in perpendicular magnetic fields^{23, 24} and shows an extremely high Curie temperature of ~ 710 K.²⁵ ζ -Mn₂N has been shown to form ζ -Fe₂N type AFM orthorhombic phase, and a neutron diffraction experiment confirmed the space group (SG) to be *Pbcn* with lattice constants $a = 5.668$ Å, $b = 4.909$ Å, and $c = 4.537$ Å.²⁶ Later, the *P6₃/mmc*-Mn₂N_{1.06} was prepared with an In–Na flux at 700 °C and 5 MPa of N₂.²⁰ η -Mn₃N₂, a tetragonal (*I4/mmm*) metal with lattice constants $a = b = 2.994$ Å, and $c = 12.499$ Å²⁷ and a Néel temperature of 925K has also been demonstrated.²⁸ Its magnetic moment is parallely aligned in the (001) plane, lies along the [100] direction, and presents an AFM order along [001]. Due to its high reversible capacity and good cycle performance, it could be used as an anode material for lithium-ion batteries.²⁹ However, the ground state structure of MnN has long been discussed. θ -MnN exists experimentally in a tetragonally distorted rock salt (*rs*) structure with AFM order. It exhibits metallic properties with lattice parameters $c/a = 0.984$ in the [001] direction, and the magnetic moment of Mn atom is 3.3 μ_B at 0 K.³⁰ However, many theories were proposed for the hypothetical cubic zinc-blende (*zb*). A. Janotti *et al*³¹ explained why the ground state *zb*-AFM state has a larger lattice constant and higher magnetic moment of the Mn atom than the FM phase. Hong *et al.* studied MnX (X= N, P, As, Sb) binary compounds in the *NiAs* and *zb* phases, and reported that their ground state is the AFM *zb* phase, because the energy of the N-*p* level is much lower than other anions *p*, and it is more likely to form a lower coordination number *zb* phase. Meanwhile, their AFM orders are larger, which reduces *p*-*d* and *d*-*d* coupling; consequently, the AFM state is more stable.³² However, compared with iron nitrides, which easily form N-rich Fe–N compounds under HP, such as FeN₂, FeN₄, Fe₃N₈, the N-rich Mn–N compounds are also worth investigating.

In this study, we investigated Mn–N compounds from 0 to 100 GPa based on *ab initio* calculations. A series of new N-rich magnetic phases were predicted. Remarkably, N-rich MnN₄ with a planar N₄ ring was discovered, and its bonding properties were analyzed, indicating that it could constitute a potentially hard superconductive material. Moreover, the phase transition sequence for MnN was updated. Finally, the incompressibility of all the structures of the Mn–N compounds was determined.

COMPUTATIONAL METHODS AND DETAILS

The structure search for Mn–N compounds were conducted based on evolutionary algorithm using the variable-composition mode of the USPEX code^{33, 34} at 0, 50, and 100 GPa. The first generation was produced randomly, and the succeeding generations were obtained by applying 50% heredity, 20% symmetric, 10% lattice mutation, and 20% soft mutation. Afterward, we fixed the ratios and varied the pressures to conduct the structural search again. Structure cells with Mn:N ratios of 3:1, 2:1, 3:2, 1:1, 1:2, and 1:4 within 1–4 formula units (f.u.) were obtained. Structural relaxations, electronic properties, and total energies were calculated using density functional theory (DFT) calculations implemented with the Vienna Ab initio Simulation Package (VASP)³⁵ with the project augmented wave method.³⁶ Additionally, the Perdew-Burke-Ernzerhof parametrization of the generalized gradient approximation was used.³⁷ A cutoff energy of 850 eV was chosen. Monkhorst-Pack k-grid meshes³⁸ with a reciprocal space resolution of $2\pi \times 0.03 \text{ \AA}^{-1}$ and $2\pi \times 0.02 \text{ \AA}^{-1}$ were used for determining the thermodynamic parameters and electronic properties, respectively. The electronic configurations of Mn and N were chosen as $3d^6 4s^1$ and $2s^2 2p^3$, respectively. Phonon dispersion curves were obtained using the PHONOPY code³⁹ based on a supercell approach with force-constant matrices and electron-phonon coupling (EPC) were performed by density functional perturbation theory as implemented in the Quantum ESPRESSO package.⁴⁰ Norm-conserving potentials were used with a kinetic energy cutoff of 90 Ry. The q-point mesh of the electron-phonon interaction matrix element adopted $4 \times 4 \times 4$ in MnN₄. Elastic constants were calculated using the strain stress method, while bulk modulus (B) and shear modulus (G) were derived from the Voigt–Reuss–Hill averaging scheme.⁴¹

Results and discussion

3.1. Phase Stability of Mn–N Compounds at High Pressure.

Formation enthalpies (ΔH_f) from the global energy minimum of the Mn–N system were computed from the convex hull. ΔH_f of each structure was calculated using the following relation: $\Delta H_f(\text{Mn}_x\text{N}_y) = [H(\text{Mn}_x\text{N}_y) - xH(\text{Mn}) - yH(\text{N})]/(x+y)$ ($x, y = 0, 1, 2, \dots$). The α -Mn and low-energy N phases (α , *Pbcn*, *P2/c*, and *cg* phases) at different pressures were used as the reference phases.⁴² From the **Figure 1a**, at 0 GPa, only Mn₃N, Mn₂N and MnN are the stable phases. The experimentally determined the cubic Mn₄N phase^{23, 43} is always above the convex hull. The lattice constants are listed in **Table S1**. In terms of structures of Mn–N compounds, with increasing nitrogen content, the hexagonal layers composed of edge-sharing NMn₆ tri-prisms in Mn-rich structures transform into polyhedral structures centered around the Mn atom in N-rich structures (**Figure S1**). The metastable phases (dynamically and mechanically stable phases, namely, NM *C2/m*-Mn₃N and NM-*Cmmm*-MnN₄) by structure search are worth studying because these are possible to be synthesized experimentally, like the AFM *Pbcn*-Mn₂N.^{4, 26} The corresponding structure diagrams are shown in **Figure S2**, and the phonon spectra are shown in **Figure S3** and **S4**. Three stable Mn-rich manganese polynitrides were predicted. For Mn₂N, experimental studies proposed a *Pbcn* phase. Examination on the relative enthalpy (**Figure S5**) reveal that

$P6_3/mmc$ - Mn_2N , obtained by structure search, has a lower energy. $R\bar{3}m$ - Mn_3N_2 is first predicted to be thermodynamically stable from 17 to 100 GPa, since $R\bar{3}m$ - Mn_3N_2 is dynamically unstable below 10 GPa; the ground state is the experimentally determined AFM- $I4/mmm$ phase at 0 GPa. $P\bar{6}m2$ - Mn_3N and $P6_3/mmc$ - Mn_2N are stable from 0 to 100 GPa. For MnN_4 , the NM- $Immm$ can be obtained by the decomposition of MnN_2 (**Figure 1b**), and it can remain stable at 40-100 GPa. From the phase diagram (**Figure 1c**), the NM- zb phase first transforms to AFM- $NiAs$ at 5 GPa, which further transforms to the more stable FM- rs phase at 40 GPa. Findings on MnN_2 will be reported in another work.

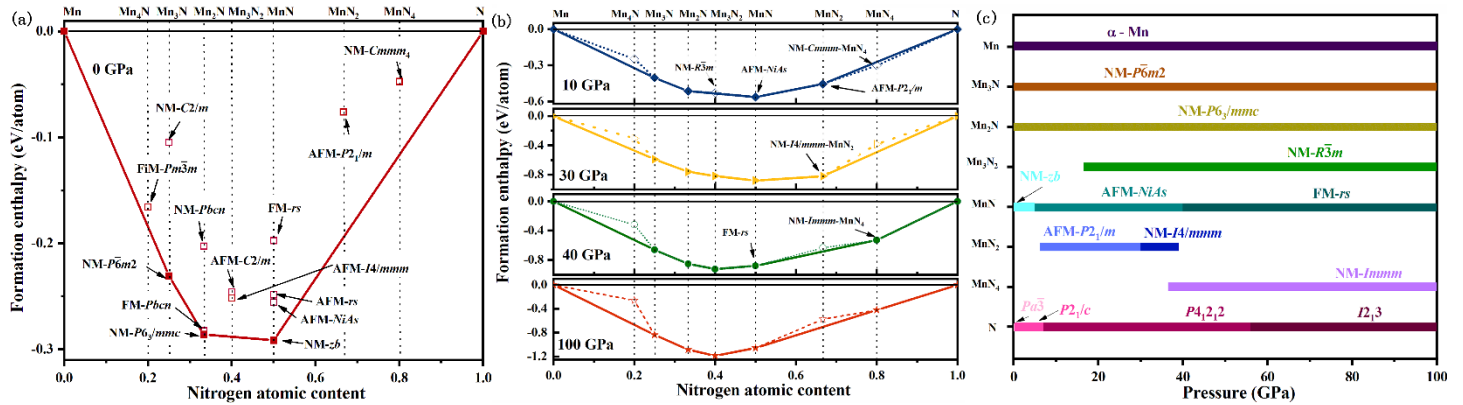


Figure 1. The magnetic phases (i.e., NM, FM, and AFM) of thermodynamic stability and the stable pressure ranges of Manganese nitrogen system. (a), (b) Convex hull diagram of the Mn–N system at different pressures at 0K. The solid squares connected by solid lines on the convex hull are represent thermodynamics and dynamics stable. (c) Pressure-composition phase diagram of the Mn–N system.

3.2. Bonding, Electronic, and Superconductive Properties of NM- $Immm$ - MnN_4 Phase with N_4 Rings

Although NM- $Immm$ - MnN_4 phase cannot be maintained at ambient pressure, the novel bonding mechanism of N atoms is worth studying. Its structure contains MnN_6 octahedrons that are connected by N atoms (**Figure 2a**). A series of poly-nitrogen forms were predicted and synthesized. Such as, the armchair-like hexazine (N_6) rings^{17, 44} the pentazolate cyclo- N_5^- ,⁴⁵⁻⁵⁰ the N_2 and N_6 unit,^{3, 4, 51} and other N-chains.^{16, 52-55} Recently, 4-membered nitrogen ring was reported in Cm - Al_2N_7 ,⁵⁶ which is similar with the nitrogen rings in $Immm$ - MnN_4 . In Al_2N_7 , there are two bond lengths of 1.36 Å and 1.37 Å respectively. And the bond lengths between N atoms are equal in MnN_4 . In **Figure 2b**, the electron local function (ELF) of this phase is calculated for bonding analysis, and it is valid for determining the bonding characteristics, such as, covalent, metallic, and ionic bonds and lone pairs. The results of ELF show strong electronic localization between adjacent N1-N2 atoms within the planar N_4 rings with a scale larger than 0.75. This implies that covalent bonds in N1-N2 and the N atoms are in the sp^2 hybridization. The N1-N2 bond length in the N_4 rings is 1.380 Å, which is extremely close to the N-N single bond at 40 GPa. The Mn-N1 and Mn-N2 bond lengths are 1.930 Å and 1.807 Å, respectively.

Moreover, the crystal orbital Hamilton population COHP (ICOHP) was analyzed to characterize the bonding in MnN_4 as depicted in **Figure 2c**. The COHP plot of the N1–N2 pairs suggests that the bonding states are fully occupied in the energy range from -12 eV to -4 eV, while the antibonding states are partially occupied, thus forming covalent bonds between N1 and N2 of the N_4 ring. There are also some covalent interactions between Mn and N due to the partial occupation of the bonding states. The value of ICOHP reflects the bond strength; the interaction between N1–N2 is the strongest (-ICOHP = 12.024); that between Mn and N1 (-ICOHP = 4.101) and Mn and N2 (-ICOHP = 2.848) are next; and the interaction between Mn-Mn (-ICOHP = 0.681) is the weakest. Furthermore, the Laplacian of the charge density at the critical point was calculated to analyze the bonding

behavior derived from the quantum theory of atoms in molecule model (QTAIM) (**Figure 2d**)⁵⁷. The bond critical points (BCPs) between N1 and the nearest N2 possess an electron density ($\rho(r)$) of 2.418 a.u. and a Laplacian ($\nabla^2\rho(r)$) of -20.255 a.u., which indicates stronger covalent interactions due to positive $\rho(r)$ and negative $\nabla^2\rho(r)$. This result is in line with COHP and ELF. The BCP between Mn and the nearest N1 (N2) atom possesses a $\rho(r)$ value of 0.678 a.u. (0.678 a.u.) and a $\nabla^2\rho(r)$ value of 14.321 a.u. (11.323 a.u.). The positive $\rho(r)$ and $\nabla^2\rho(r)$ values imply that there is not entirely closed-shell interaction between Mn and N atoms, and that there are partial charge transfer bonds.⁵⁸ In fact, the Bader charge analysis revealed that each Mn atom loses $\sim 1.2 e^-$ to adjacent N atoms.

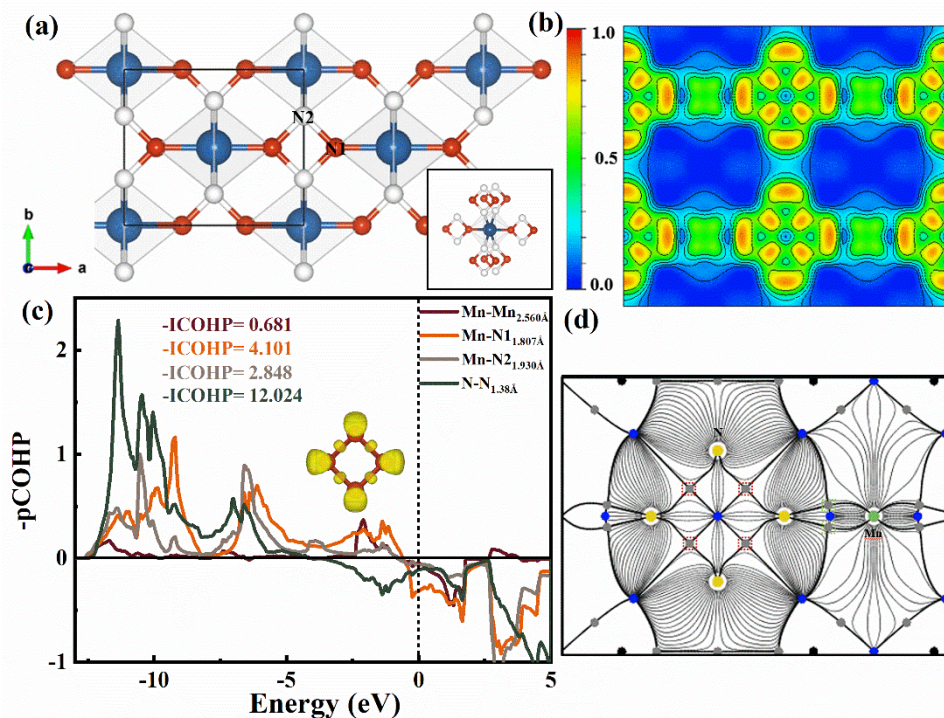


Figure 2. Crystal structures and electronic properties of MnN₄. (a) Crystal structure. Blue, red and white spheres denote Mn, N1 and N2 atoms. (b) The ELF. (c) The COHP, positive values represent bonding states, zero means nonbonding state, and negative values represent anti-bonding state. Inset represents the planer N₄ ring with an isosurface value of 0.8. (d) Gradient paths and critical points derived from QTAIM analysis for MnN₄, gray spheres represent BCPs, yellow spheres represent N, and green spheres represent Mn. Gray spheres in red dashed line boxes represent BCPs between N and N, in green dashed line boxes represent BCPs between Mn and N.

To understand the formation mechanism of the novel NM-*Immm*-MnN₄, the calculated DOS are shown in **Figure 3a**, the Mn-3*d* orbital plays a dominant role on the Fermi level and between the energy range from -13 eV to -2.5 eV, dominated by N-*p*. The *s*, *p_x*, and *p_y* orbitals of N-*p* have the same peak energy, which indicates that these orbitals of each N atoms form three *sp*² hybridized orbitals for the N₄ rings, while the two *sp*² orbitals of each N atom form two σ bonds with the *sp*² hybridized orbitals of two neighboring N atoms. The extra *sp*² orbitals form lone pairs (see the ELF in inset of **Figure 2c**), while the four *p_z* orbitals form delocalized π bonds (**Figure 3b**). The Mn-4*s* profile throughout this range of energy is very small, which indicates that charge transfer from Mn to N. Thus, the partially transferred electrons that filled the π -antibonding states impart metallicity and promote the mutual interaction between Mn and N, which results in a metallic state as well. This also confirmed the results of COHP.

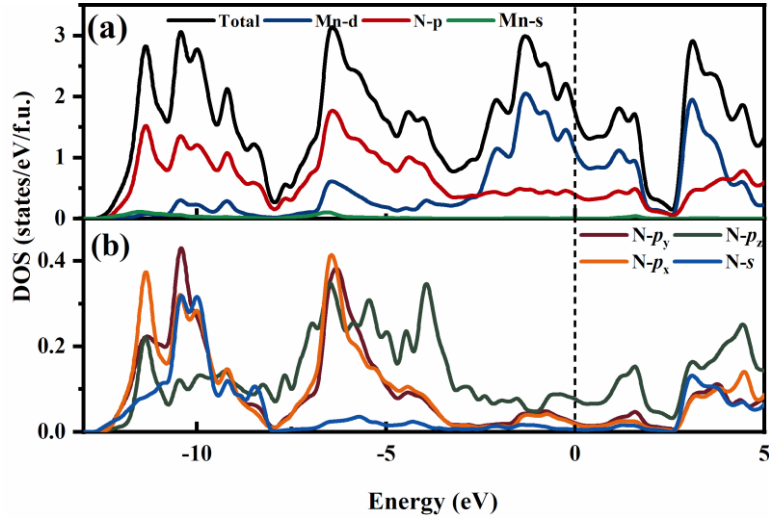


Figure 3. Projected DOS of NM-*Immm* at 40 GPa.

Due to the sizable DOS at the Fermi level of NM-*Immm*-MnN₄, we estimated the superconducting transition temperature (T_c) at 40 GPa. The phonon spectrum, PHDOS, and Eliashberg spectral function $\alpha^2F(\omega)$ together with the electron-phonon integral λ of NM-*Immm* at 40 GPa are shown in **Figure 4**. The EPC parameters, namely, $\lambda \approx 0.41$ and $T_c \approx 1.6$ K were estimated using the McMillan equation modified by Allen and Dynes⁵⁹ with a Coulomb pseudopotential $\mu^* = 0.1$.

$$T_c = \frac{\omega_m}{1.2} \exp \left[-\frac{1.04(1+\lambda)}{\lambda - \mu^*(1+0.62\lambda)} \right] \quad (1)$$

NM-*Immm*-MnN₄ has weak-coupling superconductivity. Combined with the COHP and DOS, the interaction between Mn and N is the main contribution.

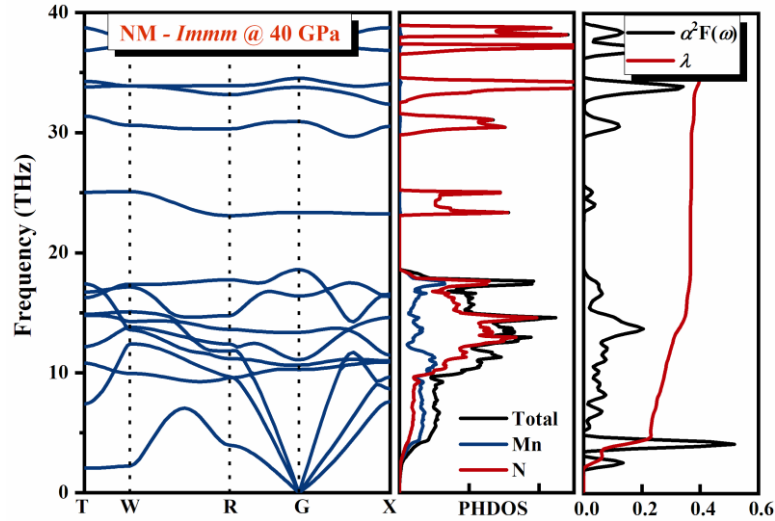


Figure 4. Phonon spectrum (left), PHDOS (middle), and Eliashberg spectral function $\alpha^2F(\omega)$ together with the electron-phonon integral λ (right) of NM-*Immm* at 40 GPa.

3.3. Phase Transformation Sequence and Electronic Properties of MnN at High Pressure

Many theoretical studies on MnN have reported that the AFM *zb*-phase should be more energetically favorable than the *rs*-phase^{32, 60, 61} similar to that observed in FeN and CoN. Miao *et al* suggested that *zb*-MnN could possibly be grown under N-rich conditions by controlled doping with S, Fe, and Co, and the transition from

zb to the stable *rs* structure was observed with 4% compression.⁶¹ However, there are no experimental reports on the *zb* phase in MnN until now. Additionally, the magnetic state of MnN continues to be discussed. Thus, we systematically studied MnN compounds from 0 to 100 GPa according to three structural stability criteria. The *zb*, *rs*, and *NiAs* structures with their magnetic phases were fully relaxed. For the experimental AFM-*rs* phase, lattice constants of $a = 4.17 \text{ \AA}$ and $c/a = 0.988$ were observed in this study, which are within the experimental values reported in the literature.³⁰ This phenomenon of lattice collapse along the *c* axis is not observed in the FM or NM phases. The relative enthalpies are shown in **Figure 5a**. In terms of energy, the AFM-*zb* phase is the ground state. However, for phonon calculation (**Figure S4**), the AFM- and FM-*zb* phases are dynamically unstable, while there are no imaginary frequencies within the NM-*zb* phase. For the *rs* phase, both the FM- and AFM phases are stable at ambient pressure. Phonon spectrum reveals that the NM-*zb* phase is more stable under negative pressure (volume expansion) than under pressure. The phonon spectrum of the AFM-*zb* phase was also calculated under negative pressure; however, this phase was still unstable. To understand this phenomenon, the electronic properties were studied (**Figure 5b, c and f**). Remarkably, the results predict the existence of a small bandgap (0.1 eV) around the Fermi level of the NM-*zb* phase, which endows poor semiconductive properties. It is attributed to the splitting of the e_g . The $d_{x^2-y^2}$ orbital is repelled above the Fermi level, while the d_z^2 orbital is pushed below the Fermi level. However, the AFM-*zb*-phase exhibits electroconductibility due to magnetic interactions, which lead to the Mn- e_g orbital contribute to the Fermi level. The N–N distance are 3.013 and 3.051 \AA in NM and AFM *zb*-phase, respectively. They are much larger than single bond N–N. Thus, we only performed the projected crystal orbital Hamilton population analysis (COHP) of MnN (**Figure 5 d and e**) to determine the structural stability. The integrated COHP (ICOHP) analysis reconfirms that the NM-*zb* phase (-ICOHP = 2.284) should be more stable than AFM- *zb* (-ICOHP = 2.041) owing to the higher bond strength. Under an increasing pressure of ~ 5 GPa, the NM-*zb* phase transforms into the AFM hexagonal *NiAs* metal. This is similar to that observed with FeN:^{16, 62} the NM-*zb* phase of FeN transforms to the FM- *NiAs* phase at ~ 24 GPa. When the pressure is higher than 40 GPa, AFM-*NiAs* has an imaginary phonon frequency. Thus, the FM-*rs*-phase appears, exhibiting metallicity (**Figure S6**). Interestingly, the phonon topology can be observed in the phonon spectrum of AFM-*NiAs* (**Figure S3 h and i**).

To summarize, the phase transition for MnN compounds proceeds in the following sequence:



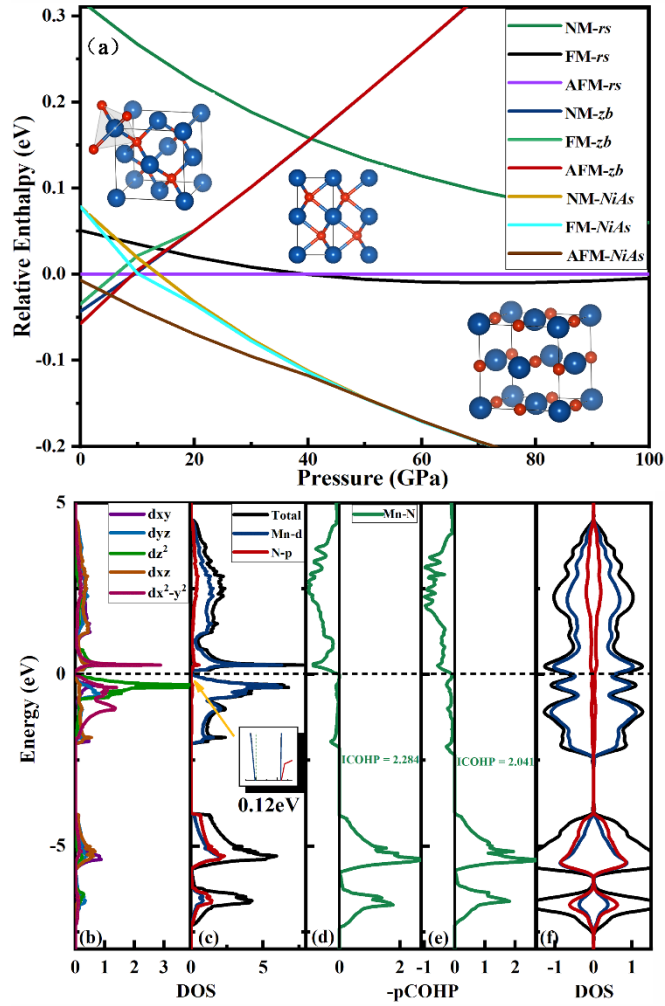


Figure 5. (a) The relative enthalpy of MnN and the insets are the crystal structures. (b - f) Electronic properties of *zb*-type MnN with NM and AFM phase at 0 GPa. The partial DOS and pCOHP (projected crystal orbital Hamilton population).

3.4. Stable Structures and Electronic Properties of Mn_3N , Mn_2N , and Mn_3N_2

Three Mn-rich phases have been predicted in the NM states, and they exist in hexagonal layers composed of edge-sharing NMn_6 tri-prisms (**Figure 6 a-c**). The difference is that the hexagonal layers are separated by the Mn layers in Mn_3N and form double tri-prisms layers with increasing N content in Mn_3N_2 . Meanwhile the crystal parameter c increased from 6.387 to 20.672 Å. The closed N-N separations are 2.587, 2.623, and 2.626 Å for the three phases and are much longer than the N-N single bond. The DOS demonstrated that these phases were remarkably metallic, and the Fermi level was dominated by the Mn-3*d* orbital. Mn-3*d* and N-2*p* exhibit the same energy peaks (−9 and −4 eV), representing a strong interaction between the N-2*p* and Mn-3*d* states. Bader charge transfer analysis reveals that each N atom of $P\bar{6}m2$ - Mn_3N gains 1.080 e^- from the Mn atoms, and Mn loses more electrons with increasing nitrogen content in the three Mn-rich structures. This, in combination with the COHP (**Figure S7**) values, reveals that the interaction between Mn and N is enhanced with increasing nitrogen content. Moreover, there are delocalized electrons between the hexagonal layers in all the three phases (**Figure 6 d-f**). This can be attributed to the metallicity of these phases.

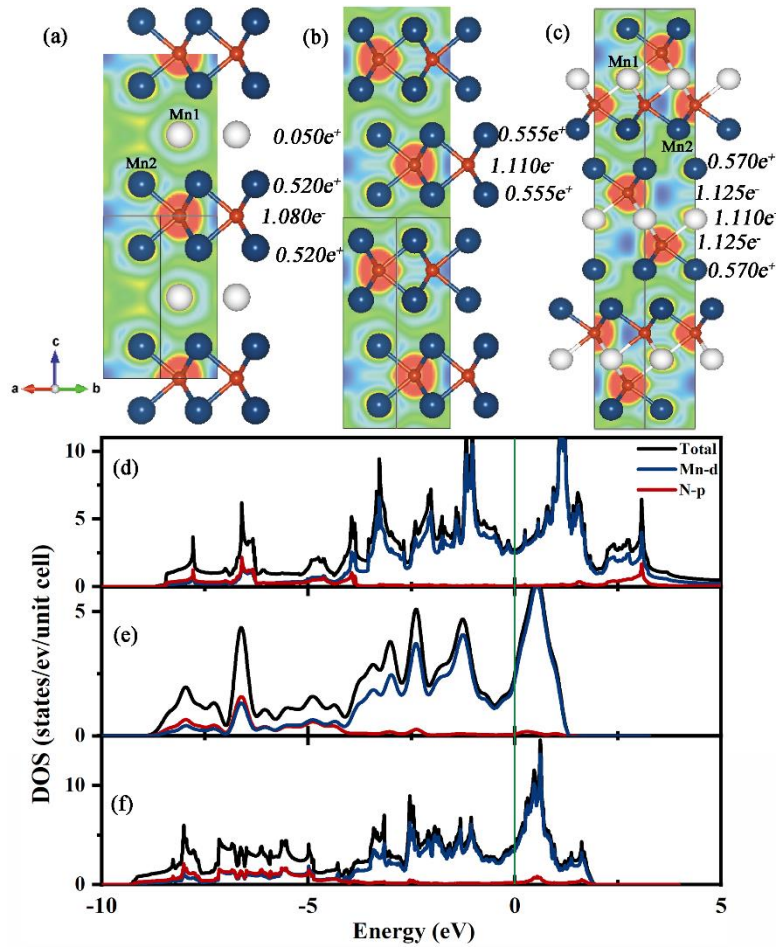


Figure 6. The structure diagrams, associated ELF contours (isosurface value = 0.65) and projected DOS of the (a) and (d) $P\bar{6}m2$ -Mn₃N at 0 GPa, (b) and (e) $P6_3/mmc$ -Mn₂N at 0 GPa and (c) and (f) $R\bar{3}m$ -Mn₃N₂ at 10 GPa.

3.5. Mechanical Properties of Mn–N compounds

Mechanical properties determine the structural stability, and TM nitrides have always exhibited outstanding incompressibility. Thus, the elastic moduli and hardness of all the Mn–N compounds were calculated and are shown in **Figure 7a** and **Table S2**. The hardness was calculated by Chen’s model (Hv1).⁶³ Due to minuscule G (39 GPa) in $NM-zb$ -MnN, the hardness is negative. Moreover, in some TM light elements, the Chen’s model may provide a hardness value that is quite different from experiment due to the lack of consideration of the metallicity and part of the covalent bond, especially in WN.^{64–66} On the contrary, the results of Zhong’s model (Hv2) agree well with the experiment. Thus, the two models were used in this work. $Immm$ -MnN₄ exhibits extremely high bulk modulus B (381 GPa) and shear modulus G (213 GPa), which can be comparable to c -BC ($B = 382$ GPa)⁶⁷. However, the hardness obtained using Chen’s model is 17.5 GPa. Considering the strong covalent bond and metallicity in MnN₄, the hardness obtained using Zhong’s model is 36 GPa, which is close to that of superhard materials (40 GPa). This can be attributed to the strong covalent bonds in the N₄ rings. AFM- $NiAs$ -MnN is also a potential hard material with hardness above 30 GPa, based on Zhong’s model. This may be attributed to the partially polar covalent bonds between Mn and N. The trend in hardness is similar to the trend in shear, G (**Figure 7b**), which changes nonlinearly with increasing nitrogen content. For the three Mn-rich phases (Mn₃N, Mn₂N, and Mn₃N₂), the hardness obtained by the two methods was consistent and slightly decreased with increasing nitrogen content. Thus, covalent interactions have a remarkable effect on the hardness of N-rich structures and almost no effect on Mn-rich structures in Mn–N compounds.

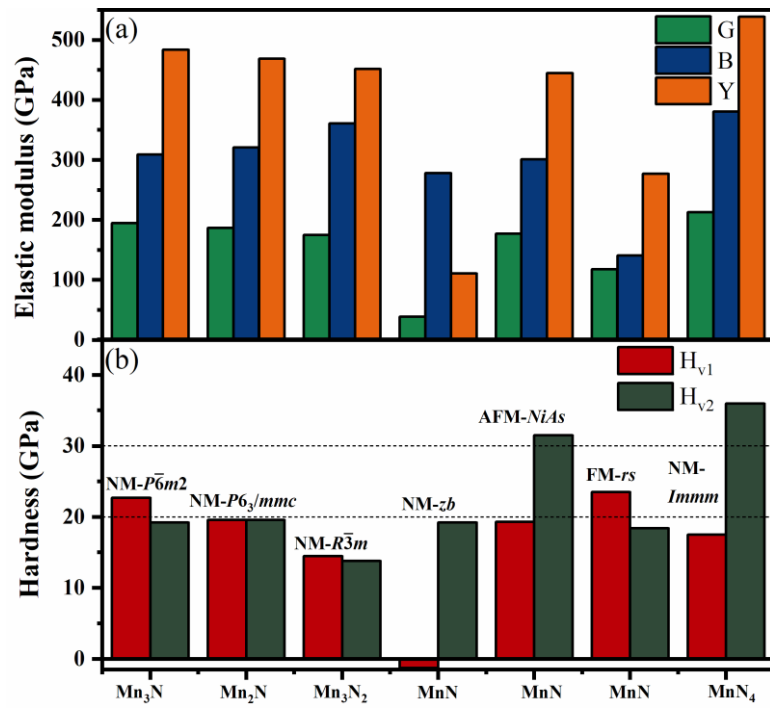


Figure 7. (a) Calculated bulk (B), shear (G) and Young's modulus (Y), (b) hardness for Mn–N compounds.

Conclusions

The crystal structures of stable Mn–N compounds were investigated systematically at 0–100 GPa. A series of thermodynamically and dynamically stable Mn–N compounds were predicted for the first time. Remarkably, N-rich MnN₄ with a planar N₄ ring and *sp*² hybridization of N was discovered for the first time. The electron occupancy of the π -antibonding states within N₄ rings and the interaction between Mn and N are attributed to the metallicity of this phase, whose $T_c \approx 1.6$ K. The strong covalent bonds in the N₄ rings play an important role in imparting the ultra-incompressible character, which renders it a hard-superconductive material. We reconstructed the phase transition sequence for manganese mononitride. The results indicated that the semi-conducting NM-*zb* (5 GPa) phase transforms to the metallic AFM-*NiAs* (40 GPa) phase, and further transforms into the more stable metallic FM-*rs* phase. AFM-*NiAs*-MnN exhibited excellent incompressibility with a hardness higher than 30 GPa, according to Zhong's model; this enables its application in harsh environments. The mechanical properties of Mn–N compounds show that covalent interactions considerably affect the hardness of N–rich structures; however, it has almost no influence on the hardness of Mn-rich structures, which raises questions on the popular models for predicting material hardness. This study on the Mn–N system may guide the syntheses of manganese–nitrogen compounds, provide a greater understanding of their properties, and aid the application of Mn–N hard multifunctional materials.

Acknowledgements

This work was supported by the National Key R&D Program of China (No. 2018YFA0703404, 2016YFB0201204, 2017YFA0403704), National Natural Science Foundation of China (Nos. 11774121, 91745203). Program for Changjiang Scholars and Innovative Research Team in University (No. IRT_15R23), Parts of calculations were performed in the High Performance Computing Center (HPCC) of Jilin University.

Supporting Information

1. Crystal structure diagrams and crystal parameters.
2. Dynamical properties of Mn-N system.
3. The relative enthalpy of Mn_2N and Mn_3N_2 .
4. The electronic properties of Mn-N system.
5. Mechanical properties of Mn-N system.

References

1. Jiang, S.; Holtgrewe, N.; Lobanov, S. S.; Su, F.; Mahmood, M. F.; McWilliams, R. S.; Goncharov, A. F. Metallization and molecular dissociation of dense fluid nitrogen. *Nat. Commun.* **2018**, 9 (1), 2624.
2. Chen, J.; Ge, Y. Emergence of intrinsic superconductivity in monolayer W_2N_3 . *Phys. Rev. B* **2021**, 103 (6).
3. Wei, S.; Li, D.; Liu, Z.; Li, X.; Tian, F.; Duan, D.; Liu, B.; Cui, T. Alkaline-earth metal (Mg) polynitrides at high pressure as possible high-energy materials. *Phys. Chem. Chem. Phys.* **2017**, 19 (13), 9246-9252.
4. Huang, B.; Frapper, G. Barium–Nitrogen Phases Under Pressure: Emergence of Structural Diversity and Nitrogen-Rich Compounds. *Chem. Mater.* **2018**, 30 (21), 7623-7636.
5. Li, D.; Tian, F.; Lv, Y.; Wei, S.; Duan, D.; Liu, B.; Cui, T. Stability of Sulfur Nitrides: A First-Principles Study. *J. Phys. Chem. C* **2017**, 121 (3), 1515-1520.
6. Peng, F.; Yao, Y.; Liu, H.; Ma, Y. Crystalline LiN_5 Predicted from First-Principles as a Possible High-Energy Material. *J. Phys. Chem. Lett.* **2015**, 6 (12), 2363-6.
7. Zhu, S.; Peng, F.; Liu, H.; Majumdar, A.; Gao, T.; Yao, Y. Stable Calcium Nitrides at Ambient and High Pressures. *Inorg. Chem. (Washington, DC, U. S.)* **2016**, 55 (15), 7550-5.
8. Han, X.; Du, H.; Guo, W. Decomposition mechanism on different surfaces of copper azide. *J Phys Condens Matter* **2021**, 33 (25).
9. Wei, S.; Li, D.; Liu, Z.; Wang, W.; Tian, F.; Bao, K.; Duan, D.; Liu, B.; Cui, T. A Novel Polymerization of Nitrogen in Beryllium Tetranitride at High Pressure. *J. Phys. Chem. C* **2017**, 121 (18), 9766-9772.
10. Yu, S.; Huang, B.; Zeng, Q.; Oganov, A. R.; Zhang, L.; Frapper, G. Emergence of Novel Polynitrogen Molecule-like Species, Covalent Chains, and Layers in Magnesium–Nitrogen Mg_xN_y Phases under High Pressure. *J. Phys. Chem. C* **2017**, 121 (21), 11037-11046.
11. Bhadram, V. S.; Kim, D. Y.; Strobel, T. A. High-Pressure Synthesis and Characterization of Incompressible Titanium Pernitride. *Chem. Mater.* **2016**, 28 (6), 1616-1620.
12. Baturina, T. I.; Mironov, A. Y.; Vinokur, V. M.; Baklanov, M. R.; Strunk, C. Localized superconductivity in the quantum-critical region of the disorder-driven superconductor-insulator transition in TiN thin films. *Phys. Rev. Lett.* **2007**, 99 (25), 257003.
13. Zou, Y.; Wang, X.; Chen, T.; Li, X.; Qi, X.; Welch, D.; Zhu, P.; Liu, B.; Cui, T.; Li, B. Hexagonal-structured epsilon-NbN: ultra-incompressibility, high shear rigidity, and a possible hard superconducting material. *Sci. Rep.* **2015**, 5, 10811.
14. Chen, X. J.; Struzhkin, V. V.; Wu, Z.; Somayazulu, M.; Qian, J.; Kung, S.; Christensen, A. N.; Zhao, Y.; Cohen, R. E.; Mao, H. K. Hard superconducting nitrides. *Proc. Natl. Acad. Sci.* **2005**, 102 (9), 3198-3201.
15. Wang, S.; Antonio, D.; Yu, X.; Zhang, J.; Cornelius, A. L.; He, D.; Zhao, Y. The Hardest Superconducting Metal Nitride. *Sci. Rep.* **2015**, 5, 13733.
16. Wu, L.; Tian, R.; Wan, B.; Liu, H.; Gong, N.; Chen, P.; Shen, T.; Yao, Y.; Gou, H.; Gao, F. Prediction of Stable Iron Nitrides at Ambient and High Pressures with Progressive Formation of New Polynitrogen Species. *Chem. Mater.* **2018**, 30 (23), 8476-8485.
17. Salke, N. P.; Xia, K.; Fu, S.; Zhang, Y.; Greenberg, E.; Prakapenka, V. B.; Liu, J.; Sun, J.; Lin, J. F. Tungsten Hexanitride with Single-Bonded Armchairlike Hexazine Structure at High Pressure. *Phys. Rev. Lett.* **2021**, 126 (6), 065702.
18. Zhao, Z.; Bao, K.; Tian, F.; Duan, D.; Liu, B.; Cui, T. Potentially superhard hcp CrN_2 compound studied at high pressure. *Phys. Rev. B* **2016**, 93 (21).
19. Suzuki, K.; Kaneko, T.; Yoshida, H.; Obi, Y.; Fujimori, H.; Morita, H. Crystal structure and magnetic properties of the compound MnN . *J. Alloys Compd.* **2000**, 306 (1-2), 66-71.
20. Aoki, M.; Yamane, H.; Shimada, M.; Kajiwara, T. Single crystal growth of Mn_2N using an In–Na flux. *Mater. Res. Bull.* **2004**, 39 (6), 827-832.
21. Jacobs, H.; Stüve, C. Hochdrucksynthese der η -phase im system Mn-N: Mn_3N_2 . *J. Less-Common Met.* **1984**, 96, 0-329.
22. Takei, W. J.; Shirane, G.; Frazer, B. C. Magnetic Structure of Mn_4N . *Physical Review* **1960**, 119 (1), 122-126.
23. Li, D.; Hu, P.; Meng, M.; Li, H.; Wu, S.; Li, S. The relation of magnetic properties and anomalous Hall

behaviors in Mn₄N (200) epitaxial films. *Mater. Res. Bull.* **2018**, 101, 162-166.

24. Li, H.; Wang, G.; Hu, P.; Li, D.; Dang, S.; Ma, X.; Dai, T.; Kang, S.; Yu, F.; Zhou, X., et al. Suppression of anomalous Hall effect by heavy-fermion in epitaxial antiperovskite Mn_{4-x}Gd_xN films. *J. Appl. Phys.* **2018**, 124 (9), 093903.

25. Meinert, M. Exchange interactions and Curie temperatures of the tetrametal nitrides Cr₄N, Mn₄N, Fe₄N, Co₄N, and Ni₄N. *J. Phys.: Condens. Matter* **2016**, 28 (5), 056006.

26. Mekata, M.; Haruna, J.; Takaki, H. Neutron Diffraction Study of Antiferromagnetic Mn₂N. *J. Phys. Soc. Jpn.* **1968**, 25 (1), 234-238.

27. Hasegawa, M.; Yagi, T. Systematic study of formation and crystal structure of 3d-transition metal nitrides synthesized in a supercritical nitrogen fluid under 10 GPa and 1800K using diamond anvil cell and YAG laser heating. *J. Alloys Compd.* **2005**, 403 (1-2), 131-142.

28. Tabuchi, M.; Takahashi, M.; Kanamaru, F. Relation between the magnetic transition temperature and magnetic moment for manganese nitrides MnN_y (0 < y < 1). *J. Alloys Compd.* **1994**, 210 (1-2), 143-148.

29. Sun, Q.; Fu, Z.-W. Mn₃N₂ as a novel negative electrode material for rechargeable lithium batteries. *Appl. Surf. Sci.* **2012**, 258 (7), 3197-3201.

30. Suzuki, K.; Yamaguchi, Y.; Kaneko, T.; Yoshida, H.; Obi, Y.; Fujimori, H.; Morita, H. Neutron Diffraction Studies of the Compounds MnN and FeN. *J. Phys. Soc. Jpn.* **2001**.

31. Janotti, A.; Wei, S.-H.; Bellaiche, L. Electronic and magnetic properties of MnN versus MnAs. *Appl. Phys. Lett.* **2003**, 82 (5), 766-768.

32. Hong, H.-M.; Kang, Y.-J.; Kang, J.; Lee, E. C.; Kim, Y. H.; Chang, K. J. Effect of chemical bonding on the magnetic stability and magnetic moment in Mn-based binary compounds. *Phys. Rev. B* **2005**, 72 (14).

33. Lyakhov, A. O.; Oganov, A. R.; Stokes, H. T.; Zhu, Q. New developments in evolutionary structure prediction algorithm USPEX. *Comput. Phys. Commun.* **2013**, 184 (4), 1172-1182.

34. Oganov, A. R.; Lyakhov, A. O.; Valle, M. How Evolutionary Crystal Structure Prediction Works—and Why. *Acc. Chem. Res.* **2010**, 44 (3), 227-237.

35. Kresse, G.; Furthmüller, J. Efficient iterative schemes for ab initio total-energy calculations using a plane-wave basis set. *Phys. Rev. B* **1996**, 54 (16), 11169.

36. Kresse, G.; Joubert, D. From ultrasoft pseudopotentials to the projector augmented-wave method. *Phys. Rev. B* **1999**, 59 (3), 1758.

37. Perdew, J. P.; Burke, K.; Ernzerhof, M. Generalized Gradient Approximation Made Simple. *Phys. Rev. Lett.* **1996**, 77 (18), 3865--3868.

38. Monkhorst, H. J.; Pack, J. D. Special points for Brillouin-zone integrations. *Phys. Rev. B* **1976**, 13 (12), 5188.

39. Togo, A.; Oba, F.; Tanaka, I. First-principles calculations of the ferroelastic transition between rutile-type and CaCl₂-type SiO₂ at high pressures. *Phys. Rev. B* **2008**, 78 (13).

40. Giannozzi, P.; Baroni, S.; Bonini, N.; Calandra, M.; Car, R.; Cavazzoni, C.; Ceresoli, D.; Chiarotti, G. L.; Cococcioni, M.; Dabo, I. QUANTUM ESPRESSO: a modular and open-source software project for quantum simulations of materials. *J. Phys.: Condens. Matter* **2009**.

41. Hill. The Elastic Behaviour of a Crystalline Aggregate. *Proc. Phys. Soc.* **1952**, 65 (5), 349-354.

42. Pickard, C. J.; Needs, R. J. High-pressure phases of nitrogen. *Phys. Rev. Lett.* **2009**, 102 (12), 125702.

43. Mekata, M. Magnetic Study on Mn₄N and its Related Compounds. *J. Phys. Soc. Jpn.* **1962**, 17 (5), 796-803.

44. Williams, A. S.; Steele, B. A.; Oleynik, II. Novel rubidium poly-nitrogen materials at high pressure. *J. Chem. Phys.* **2017**, 147 (23), 234701.

45. Liu, Z.; Li, D.; Tian, F.; Duan, D.; Li, H.; Cui, T. Moderate Pressure Stabilized Pentazolate Cyclo-N₅(-) Anion in Zn(N₅)₂ Salt. *Inorg. Chem. (Washington, DC, U. S.)* **2020**, 59 (12), 8002-8012.

46. Xu, Y.; Wang, Q.; Shen, C.; Lin, Q.; Wang, P.; Lu, M. A series of energetic metal pentazolate hydrates. *Nature* **2017**, 549 (7670), 78-81.

47. Chong, Z.; Chengguo, S.; Bingcheng, H.; Chuanming, Y.; Ming, L. Synthesis and characterization of the pentazolate anion cyclo-N₅⁻ in (N₅)₆(H₃O)₃(NH₄)₄Cl. *Science* **2020**, 355, 374-376.

48. Zhang, C.; Yang, C.; Hu, B.; Yu, C.; Zheng, Z.; Sun, C. A Symmetric Co(N₅)₂(H₂O)₄·4H₂O High-Nitrogen Compound Formed by Cobalt(II) Cation Trapping of a Cyclo-N₅⁻ Anion. *Angew. Chem., Int. Ed.* **2017**, 56 (16),

4512-4514.

49. Laniel, D.; Weck, G.; Gaiffe, G.; Garbarino, G.; Loubeyre, P. High-Pressure Synthesized Lithium Pentazolate Compound Metastable under Ambient Conditions. *J. Phys. Chem. Lett.* **2018**, *9* (7), 1600-1604.
50. Arhangelskis, M.; Katsenis, A. D.; Morris, A. J.; Friscic, T. Computational evaluation of metal pentazolate frameworks: inorganic analogues of azolate metal-organic frameworks. *Chemical Science* **2018**, *9* (13), 3367-3375.
51. Kvashnin, A. G.; Oganov, A. R.; Samtsevich, A. I.; Allahyari, Z. Computational Search for Novel Hard Chromium-Based Materials. *J. Phys. Chem. Lett.* **2017**, *8* (4), 755-764.
52. Zhang, J.; Oganov, A. R.; Li, X.; Niu, H. Pressure-stabilized hafnium nitrides and their properties. *Phys. Rev. B* **2017**, *95* (2).
53. Zhao, Z.; Bao, K.; Tian, F.; Duan, D.; Liu, B.; Cui, T. Phase diagram, mechanical properties, and electronic structure of Nb-N compounds under pressure. *Phys. Chem. Chem. Phys.* **2015**, *17* (35), 22837-45.
54. Miao, J.-Y.; Lu, Z.-S.; Peng, F.; Lu, C. New Members of High-Energy-Density Compounds: YN₅ and YN₈. *Chin. Phys. Lett.* **2021**, *38* (6), 066201.
55. Liu, Z.; Li, D.; Wei, S.; Liu, Y.; Tian, F.; Duan, D.; Cui, T. Nitrogen-rich GaN₅ and GaN₆ as high energy density materials with modest synthesis condition. *Phys. Lett. A* **2019**, *383* (28), 125859.
56. Du, H.; Ge, Y.; Zhu, J.; Guo, W.; Yao, Y. Pressure-induced novel nitrogen-rich aluminum nitrides: AlN₆, Al₂N₇ and AlN₇ with polymeric nitrogen chains and rings. *Phys. Chem. Chem. Phys.* **2021**, *23* (21), 12350-12359.
57. Vega, D.; Almeida, D. AIM-UC: An application for QTAIM analysis. *J. Comput. Methods Sci. Eng.* **2014**, *14* (1-3), 131-136.
58. Rzepa, H. The weirdest bond of all? Laplacian isosurfaces for [1.1.1]Propellane. *Henry Rzepa* **2010**.
59. Allen, P. B.; Dynes, R. C. Transition temperature of strong-coupled superconductors reanalyzed. *Phys. Rev. B* **1975**, *12* (3), 905-922.
60. Miao, M. S.; Lambrecht, W. R. L. Effects of vacancies and impurities on the relative stability of rocksalt and zincblende structures for MnN. *Phys. Rev. B* **2007**, *76* (19).
61. Miao, M. S.; Lambrecht, W. R. L. Structure and magnetic properties of MnN, CrN, and VN under volume expansion. *Phys. Rev. B* **2005**, *71* (21).
62. Clark, W. P.; Steinberg, S.; Dronskowski, R.; McCammon, C.; Kuppenko, I.; Bykov, M.; Dubrovinsky, L.; Akselrud, L. G.; Schwarz, U.; Niewa, R. High-Pressure NiAs-Type Modification of FeN. *Angew Chem Int Ed Engl* **2017**, *56* (25), 7302-7306.
63. Chen, X.-Q.; Niu, H.; Li, D.; Li, Y. Modeling hardness of polycrystalline materials and bulk metallic glasses. *Intermetallics* **2011**, *19* (9), 1275-1281.
64. Zhong, M.-M.; Kuang, X.-Y.; Wang, Z.-H.; Shao, P.; Ding, L.-P.; Huang, X.-F. Phase Stability, Physical Properties, and Hardness of Transition-Metal Diborides MB₂ (M = Tc, W, Re, and Os): First-Principles Investigations. *J. Phys. Chem. C* **2013**, *117* (20), 10643-10652.
65. Feng, X.; Bao, K.; Tao, Q.; Li, L.; Shao, Z.; Yu, H.; Xu, C.; Ma, S.; Lian, M.; Zhao, X., et al. Role of TM-TM Connection Induced by Opposite d-Electron States on the Hardness of Transition-Metal (TM = Cr, W) Mononitrides. *Inorg. Chem. (Washington, DC, U. S.)* **2019**, *58* (22), 15573-15579.
66. Xu, C.; Bao, K.; Ma, S.; Li, D.; Duan, D.; Yu, H.; Jin, X.; Tian, F.; Liu, B.; Cui, T. Revealing unusual rigid diamond net analogues in superhard titanium carbides. *RSC Advances* **2018**, *8* (26), 14479-14487.
67. Yakovenko, E.; Aleksandrov, I.; Goncharov, A.; Stishov, S. Cubic boron nitride at high pressures: equation of state and Raman light scattering. *Zh. Eksp. Teor. Fiz.* **1989**, *95* (6), 2097-2102.

TOC Graph

